

Key Points:

- Transition of elastic to inelastic deformation was explored in the Abarkuh Plain (AP) from Interferometric Synthetic Aperture Radar Time Series
- The boundary of the confined aquifer was defined from seasonal deformation
- The AP has experienced a rapid expansion of inelastic deformation areas in less than two decades

Supporting Information:

Supporting Information may be found in the online version of this article.

Correspondence to:

S. Jin,
sgjin@shao.ac.cn;
sg.jin@yahoo.com

Citation:








Mirzadeh, S. M. J., Jin, S., Chaussard, E., Bürgmann, R., Rezaei, A., Ghotbi, S., & Braun, A. (2023). Transition and drivers of elastic to inelastic deformation in the Abarkuh Plain from InSAR multi-sensor time series and hydrogeological data. *Journal of Geophysical Research: Solid Earth*, 128, e2023JB026430. <https://doi.org/10.1029/2023JB026430>

Received 26 JUN 2022
 Accepted 21 JUN 2023

Author Contributions:

Conceptualization: Sayyed Mohammad Javad Mirzadeh, Shuanggen Jin
Data curation: Sayyed Mohammad Javad Mirzadeh, Saba Ghotbi, Andreas Braun
Formal analysis: Sayyed Mohammad Javad Mirzadeh
Funding acquisition: Shuanggen Jin
Investigation: Sayyed Mohammad Javad Mirzadeh, Shuanggen Jin, Estelle Chaussard, Roland Bürgmann
Methodology: Sayyed Mohammad Javad Mirzadeh, Shuanggen Jin, Estelle Chaussard, Roland Bürgmann
Project Administration: Shuanggen Jin
Resources: Sayyed Mohammad Javad Mirzadeh, Saba Ghotbi, Andreas Braun
Software: Sayyed Mohammad Javad Mirzadeh, Saba Ghotbi

Transition and Drivers of Elastic to Inelastic Deformation in the Abarkuh Plain From InSAR Multi-Sensor Time Series and Hydrogeological Data

Sayyed Mohammad Javad Mirzadeh^{1,2} , Shuanggen Jin^{1,3} , Estelle Chaussard⁴ , Roland Bürgmann⁵ , Abolfazl Rezaei^{6,7} , Saba Ghotbi⁸ , and Andreas Braun⁹ 

¹Shanghai Astronomical Observatory, Chinese Academy of Sciences, Shanghai, China, ²School of Astronomy and Space Science, University of Chinese Academy of Sciences, Beijing, China, ³School of Surveying and Land Information Engineering, Henan Polytechnic University, Jiaozuo, China, ⁴Independent Researcher, Boston, MA, USA, ⁵Department of Earth and Planetary Science, University of California Berkeley, Berkeley, CA, USA, ⁶Department of Earth Sciences, Institute for Advanced Studies in Basic Sciences (IASBS), Zanjan, Iran, ⁷Center for Research in Climate Change and Global Warming (CRCC), Institute for Advanced Studies in Basic Sciences (IASBS), Zanjan, Iran, ⁸Singhofen and Associates Incorporated, Orlando, FL, USA, ⁹Department of Geography, University of Tübingen, Tübingen, Germany

Abstract Tracking the inelastic deformation of an aquifer is important to quantify the stress experienced by the aquifer system, so that the effects of the current extraction practices are put in the context of the hydrogeological settings of a region. However, transition of elastic to inelastic deformation is hard to be monitored, particularly in the Abarkuh Plain (AP) with a dry climate. In this study, we define the confined extent of aquifer system and track the spatial evolution of inelastic deformation based on the multi-sensor Interferometric Synthetic Aperture Radar time series in the AP in central Iran from 2003 to 2020. Our results demonstrate that many locations with experiencing no significant inelastic deformation a few years ago are now deforming inelastically, leading to partially irreversible lowering of ground surface and loss of aquifer storage. Lithological data shows that total thickness of compacted clay units controls the extent and timing of observed inelastic deformation, while joint geodetic-well data confirms that multi-decadal dropping of head in the confined extents of aquifer system is driving the long-term compaction. These results show that we are possibly near a tipping point between the sustainable conditions and permanent damage to underground water resources and the current decisions have the potential to permanently change the natural resources landscape.

Plain Language Summary Unsustainable extraction of groundwater is accompanied by inelastic land subsidence, lowering of surface elevation. Tracking the transition of elastic to inelastic deformation is critical to isolating a tipping point between sustainability and permanent damage to underground water resources. In this work, we present an approach based on the space geodesy to quantify the transition and spatial evolution of inelastic deformation. Our study reveals that many locations in central Iran that used to experience no significant inelastic deformation just a few years ago, are now deforming inelastically, leading to the significant subsidence and partially loss of the aquifer system storage. We find that while compaction is associated with multi-decadal groundwater levels decline, nature and thickness of sediments in the subsurface relative to local groundwater elevation control its timing. These results highlight the fact that recent and current groundwater management decisions have the potential to change the natural resources landscape permanently in central Iran.

1. Introduction

In an aquifer system, both inelastic (irreversible) and elastic (recoverable) deformation take place (Wilson & Gorelick, 1996), relating to hydraulic head fluctuations, properties of deforming sediment layers, and the aquifer's compaction history (Poland & Ireland, 1988). As long as the hydraulic head remains above the previous lowest level (i.e., the effective stress is less than the pre-consolidation stress), the deformation is elastic and takes place in both fine- and coarse-grained layers (Sneed, 2001). In contrast, when the hydraulic head falls below its previous lowest level, inelastic compaction is initiated predominantly in clay layers through irreversible rearrangement of fine grains. Compaction is greater in clays than in coarse sediments due to the inelastic skeletal specific storage being one-to-three orders of magnitude greater than the elastic skeletal specific storage (Guzy & Malinowska, 2020). Since inelastic and elastic processes often simultaneously happen in the same place, their

Supervision: Shuanggen Jin

Validation: Sayyed Mohammad Javad Mirzadeh, Shuanggen Jin, Estelle Chaussard, Roland Bürgmann, Abolfazl Rezaei

Visualization: Sayyed Mohammad Javad Mirzadeh

Writing – original draft: Sayyed Mohammad Javad Mirzadeh

Writing – review & editing: Sayyed Mohammad Javad Mirzadeh, Shuanggen Jin, Estelle Chaussard, Roland Bürgmann, Abolfazl Rezaei, Saba Ghotbi, Andreas Braun

separation is challenging without relying upon the hydrogeological models (Hoffmann et al., 2003). However, quantifying these deformation components is essential to define sustainable pumping rates for resources management and to potentially relocate infrastructures from the areas experiencing inelastic deformation (Shi et al., 2012).

Interferometric Synthetic Aperture Radar (InSAR) can quantify surface deformation from small to very large extents worldwide (tens to thousands of square kilometers) with a high-spatial resolution (tens of meters) (Chang et al., 2014; Pepe & Calò, 2017). Ground deformation linked to subsurface and solid-earth processes can be precisely measured with InSAR and explored to gain insights into the physical and hydro-mechanical processes at play (e.g., Bürgmann et al., 2000). InSAR has been broadly applied in the hydrogeology to derive the properties of aquifer systems and to guide water-storage management plans (Chaussard et al., 2021; Ezquerro et al., 2014; Lu & Danskin, 2001; Miller & Shirzaei, 2015; Rezaei & Mousavi, 2019).

Characterization of land deformation has been documented in several plains or sedimentary basins such as the Las Vegas Valley, Nevada, USA (Hoffmann et al., 2001), the Parowan Valley, Utah, USA (Smith & Li, 2021), the San Joaquin Valley and San Bernardino Basin, California, USA (Lu & Danskin, 2001; Smith & Knight, 2019), the San Luis Valley, Colorado, USA (J. Chen et al., 2017), the Phoenix and Tucson, Arizona, USA (Miller et al., 2017; Miller & Shirzaei, 2015), the Guadalentín Valley, Spain (Rigo et al., 2013), the Toluca Valley, Mexico (Calderhead et al., 2011), the National Capital Region (NCR), India (Kumar et al., 2022), the Cangzhou, North China Plain and Xi'an (Jiang et al., 2018; Li et al., 2023), and the Rafsanjan, Gorgan, and Salmas Plains, Iran (Motagh et al., 2017; Rezaei & Mousavi, 2019; Shahbazi et al., 2022). Chaussard et al. (2014, 2017) discovered land subsidence in the Santa Clara aquifer, CA, and presented that the elastic deformation can be spatiotemporally complex and reach amplitudes of centimeters each year. Ojha et al. (2019) studied vertical land deformation in the Central Valley, CA, with a 2015–2017 InSAR time series and used a functional curve fitting to isolate elastic from inelastic contributions, assuming the elastic component can be seasonal. Ezquerro et al. (2014) and Haghighi and Motagh (2019) reported land motion in Madrid, Spain and Tehran, Iran, respectively, with multi-sensor InSAR deformation time series, and isolated inelastic from elastic contributions, assuming inelastic component can be a long-term linear trend. Using an Independent Component Analysis (ICA) of the Sentinel-1 InSAR time series, Chaussard et al. (2021) and Mirzadeh et al. (2021) highlighted the detail of the inelastic and elastic deformations in the Mexico City and Yazd-Ardakan Plain, Iran, respectively. At both sites, surface deformation was shown to be dominantly inelastic and controlled by clay-layers thickness that compact in response to water levels dropping below the previous lowest stands. Gualandi and Liu (2021) used variational Bayesian ICA (vbICA) and 2015–2019 Sentinel-1 time series across the Central San Andreas Fault and southern Central Valley to isolate the contributions of deep and shallow aquifer deformation to displacements and distinct tectonic loading from the seasonal signals. Peng et al. (2022) applied an ICA to 2006–2020 time series of displacement from the ALOS-1 and Sentinel-1 data sets across the Willcox basin in Arizona and discovered two various spatiotemporal deformation zones in this basin. Using 2016–2018 InSAR observations, Y. Chen et al. (2022) showed the spatiotemporal pattern of land motion in Lingang New City, Shanghai and discovered elastic and inelastic deformation through calculating the skeleton coefficients by the joint analysis of hydraulic head data and InSAR results. Zhu et al. (2022) applied an ICA to the 2015–2018 Sentinel-1 InSAR time series in the Santa Ana basin, Los Angeles, and discovered two various spatiotemporal deformation patterns in the basin; a long-term deformation zone with the large-scale pattern and a widespread seasonal deformation linked to the seasonal groundwater level changes. Smith and Li (2021) presented a new approach to model the elastic and inelastic deformation using the incomplete water level records and 2015–2020 Sentinel-1 deformation data across the Parowan Valley, Utah and found the deformation at the study site as a mixture of continued year-over-year drawdown and large seasonal variations in head. Lees et al. (2022) and Smith and Knight (2019) used the 1D groundwater flow (i.e., diffusion equation) in the San Joaquin Valley, California, that uses the hydraulic parameters and changes in head (i.e., stress) at the border of fine-grained units layers experiencing the inelastic land deformations, to estimate the deformation experienced by the clay layers in response to significant aquifer storage depletion. Jiang et al. (2018) applied multichannel singular spectrum analysis (M-SSA) to 2003–2010 InSAR observations and hydraulic head changes to extract seasonal signal, and then estimate the elastic skeletal storativity, aquifer parameters and groundwater storage variations in Cangzhou, North China Plain. Shi et al. (2022) used a continuous wavelet transform to separate the seasonal and long-term components of 2015–2020 InSAR deformation time series and hydraulic measurements and then retrieved aquifer storage parameters in the Tianjin–Langfang area, North China Plain.

Although multi-sensor InSAR deformation time series data have been used worldwide to track the aquifer-related deformation, most have relied on a relatively short period of observations, which does not enable isolation the

transition between the elastic and inelastic surface deformation (Bai et al., 2022; Chaussard et al., 2021; Hu et al., 2018; Mirzadeh et al., 2021; Peng et al., 2022; Song et al., 2022). Recent studies that combine InSAR time series of the historical and recent SAR missions have assumed constant deformation rates in all periods when merging the time series or have used quantile–quantile adjustment and segmented linear interpolation methods, which are not applicable in all cases and often result in large uncertainties in the estimations of recoverable and irrecoverable storage values (Aimaiti et al., 2018; Li et al., 2023; Motagh et al., 2017; Wang et al., 2021).

In this paper, we extract the time-dependent evolution of the inelastic deformation through implementation of multi-sensor long-term time series analysis from both historical and recent SAR data combined with an ICA. The ICA enables exploring any time and space variability that may be embedded in the InSAR data and hidden by the dominant signal without relying on a prior constraints and prescribed functional forms. We focus on the Abarkuh Plain (AP), Iran, and resolve the primary controls by the hydrogeological factors of the spatiotemporally variable transition of elastic to inelastic deformation. We rely on a joint analysis of hydrogeological and geodetic data to constrain the spatial extent of the confined aquifer in the AP, which was unknown to this day, and track the locations of the AP that have switched from experiencing purely elastic deformation to facing some inelastic deformation in recent years due to the continued lowering of groundwater levels.

2. Study Area and Hydrogeology

The AP is a desert extending from 52.67 to 53.72°E longitude and 30.68 and 31.50°N latitude. Its elevation increases from 1,439 m in the Abarkuh Playa in the southeast to 3,277 m in mountains to the west (Figure 1a). According to 1967–2011 data, the AP has an average annual rainfall of ~ 464.6 million m^3 and an annual evaporation of ~ 377.78 million m^3 (TAMAB, 2004). The AP is made up of one unconfined aquifer extending from the surface to shallow depths, which covers an area of 929.12 km^2 (Figure 1a) and has suffered from an average yearly decline of groundwater levels of 0.62 m between 1983 and 2017 (TAMAB, 2004). Underneath, a confined aquifer system has been suggested in the AP but its spatial extent remains unclear. The long-term (1981–2011) groundwater budget in the AP shows that the main component of recharge arises from the direct percolation and irrigation return flow from the agricultural sector at 61.1 million m^3 per year. Withdrawal by springs, qanats, and pumping wells reaches 173.7 million m^3 per year, with the largest usage stemming from agricultural activities that extract 168.1 million m^3 of water per year (Tables S1 and S2 in Supporting Information S2). The yearly storage loss of 32.4 million m^3 has led the local government to label the AP aquifer as the second-most imperiled aquifer in this region (TAMAB, 2004).

Figure 1a shows the geology of the AP. Quaternary sediments cover much of the area, consisting of alluvium (clays, silts, and sand along with gypsum) and salt flats. These Quaternary layers are underlain by Tertiary to Permian limestone and dolomite units and the thickness changes are controlled by several NWSE- and NS-trend strike-slip faults (profile A–A' and the lithological data from several exploration wells in Figure 1b and Figure S1 in Supporting Information S1, respectively).

3. Data Sets and Methods

3.1. Data Sets

3.1.1. SAR Data

Our analysis is based on 12 Envisat ASAR images of the AP acquired in StripMap (SM) mode, 14 ALOS-1 PALSAR images acquired in Fine Beam Double (FBD) Polarization and Fine Beam Single (FBS) Polarization modes, and 243 Sentinel-1 images acquired in the Interferometric Wide-swath (IW) mode (inset map in Figure 1a). The Envisat descending data was acquired from October 2003 to September 2005 with a resolution of $4 \times 8 \text{ m}^2$ (Azimuth \times Range). The ALOS-1 ascending data was acquired from December 2006 to December 2010 with a resolution of $3 \times 8 \text{ m}^2$ (Azimuth \times Range) (Table S3 in Supporting Information S2). The Sentinel-1 data set in both descending and ascending orbits cover a period from October 2014 to March 2020 with a spatial resolution of $20 \times 5 \text{ m}^2$ (Azimuth \times Range) (Table S4 in Supporting Information S2).

3.1.2. Hydrogeological, and GNSS Data

We use monthly measurements from 28 piezometers (red dots in Figure 1a) to quantify the hydraulic head variations from March 2003 to March 2020, considering March 2003 as the reference date (Figure S2 in Supporting Information S1). We apply an Inverse Distance Weighted (IDW) interpolation method (Shepard, 1968) on the measurements from the piezometers to generate multi-annual hydraulic head change maps between October

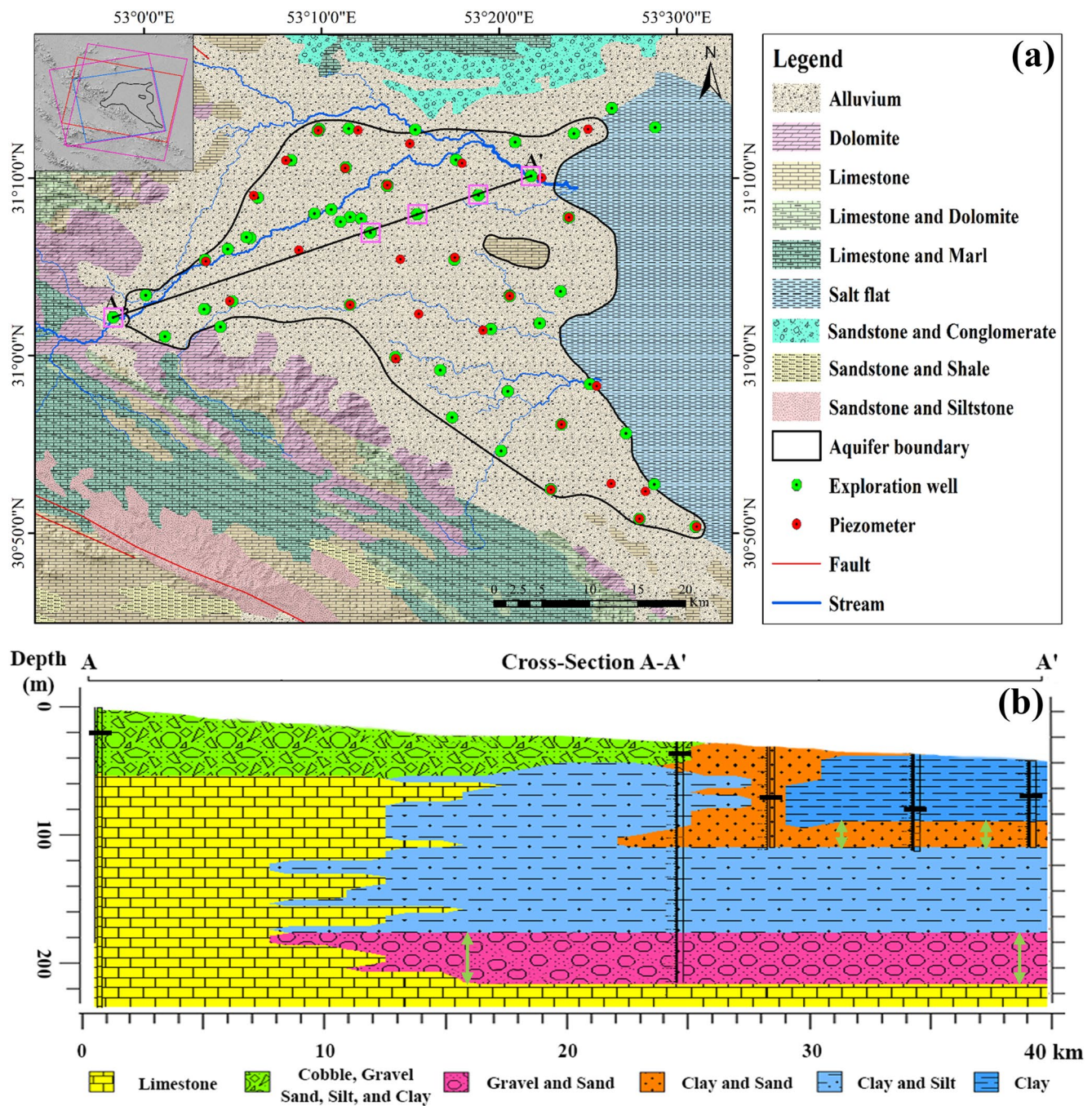


Figure 1. (a) Geological map of the Abarkuh Plain at a scale of 1:100,000, converted from the Geological Survey of Iran (1997). Dark outlines denote the boundary of aquifer. Green and red dots display the locations of available exploration wells and piezometers, respectively. The A–A' line shows the location of SW–NE cross-section. The inset map shows outlines of frames from the Envisat descending, ALOS-1 ascending, and the Sentinel-1 descending and ascending orbit directions in red, blue, and pink, respectively, overlaying a hillshade map. (b) Geological cross-section of the aquifer along profile A–A' using data from five exploration wells highlighted in (a) by pink squares. The black horizontal lines display the water table at the end of drilling process of exploration wells. The green vertical double arrows show the thickness of those parts of the aquifer system that are potentially confined. The bedrock is made of limestone units (yellow) and the aquifer unit's thicknesses atop (i.e., all non-limestone layers) decrease eastward.

2003, considered as the reference date, and consecutive years (2004–2019; Figure S3 in Supporting Information S1), as well as the annual hydraulic head change maps in the periods of the Envisat, ALOS-1 and Sentinel-1 data sets (Figure S4 in Supporting Information S1). October is considered as the start of the hydrological year. Logs data of several exploration wells (green dots in Figure 1a; TAMAB, 2004) are used to derive the lithological

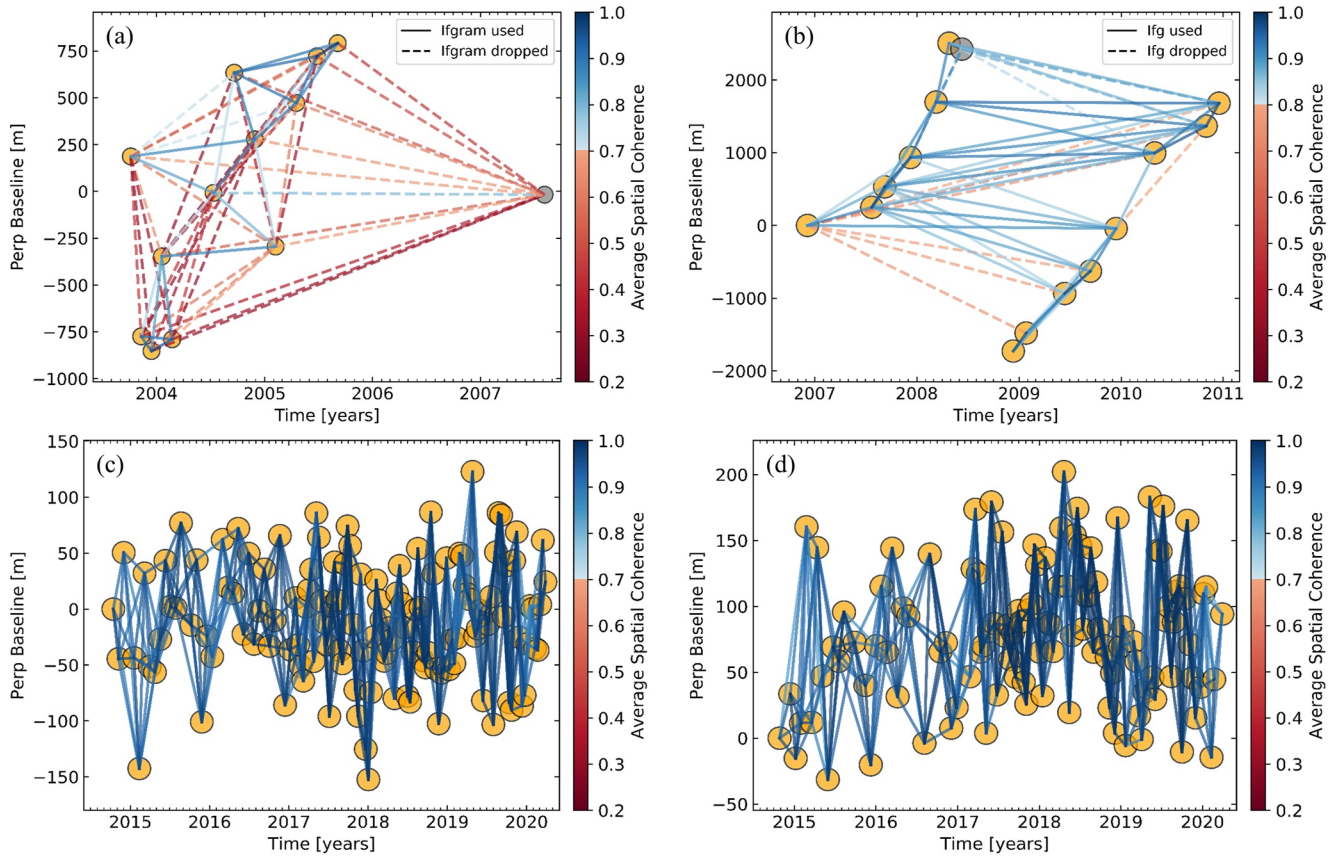


Figure 2. Spatial (perpendicular) and temporal baselines of the Envisat (a), ALOS-1 (b), and the Sentinel-1 ascending (c) and descending (d) interferograms color-coded by the average spatial coherence. Dashed lines in (a and b) show interferograms ignored when applying the average spatial coherence thresholds to the time series selection and the solid lines in (a–d) demonstrate interferograms inverted to get the time series of land deformation.

information from the upper ~ 100 m (Figure S1 in Supporting Information S1). Stratigraphic data of the AP are also derived from the geological map at a scale of 1:100,000 (Geological Survey of Iran, 1997).

Global Navigation Satellite System (GNSS) can monitor multi-scale deformation and the water storage variations (Jin et al., 2022; Jin & Zhang, 2016; Najibi & Jin, 2013). One continuous GNSS station of the Iranian Permanent GNSS Network (IPGN) provided by the National Cartography Center of Iran (NCC) is available in the AP (see its location in Figure 3 with the black triangle). This GNSS station (ABRK) provides daily data since 2006 in the form of time series of 3D positions (E–W, N–S, and Up–Down) processed at NCC using the GAMIT/GLOBK software (Herring et al., 2015) in the International Terrestrial Reference Frame, ITRF2014 (see Figure S5 in Supporting Information S1). We consider the first acquisition date (1 January 2006) as the reference of the displacement time series.

3.2. Methods

3.2.1. InSAR Approach

To track ground deformation over the period covered by each SAR data set, we use the InSAR Scientific Computing Environment software and Small Baseline Subset (SBAS; Berardino et al., 2002) time series method implemented in the Miami INsar Time-series software in PYTHON (MintPy; Yunjun et al., 2019). We set perpendicular and temporal baseline thresholds to 1,070 m and 1,800 days for the Envisat and 1,500 m and 1,800 days for the ALOS-1 data sets to produce over 63 and 57 interferograms, respectively (see Figure 2). For the Sentinel-1 ascending and descending data sets, we generate over 506 and 446 interferograms, respectively, formed between each epoch and four preceding and four subsequent epochs with temporal and spatial baselines between 12 and 168 days and -200 and 200 m (see Figure 2). We rely on the 1-arcsec Digital Elevation Model (DEM) of the Shuttle Radar Topography Mission (SRTM; Jarvis et al., 2008) to limit the topographical contributions. We resample the interferograms to 90 m for the Envisat and ALOS-1, and 30 m for the Sentinel-1 data sets to reduce the speckle noise and use the Statistical-Cost

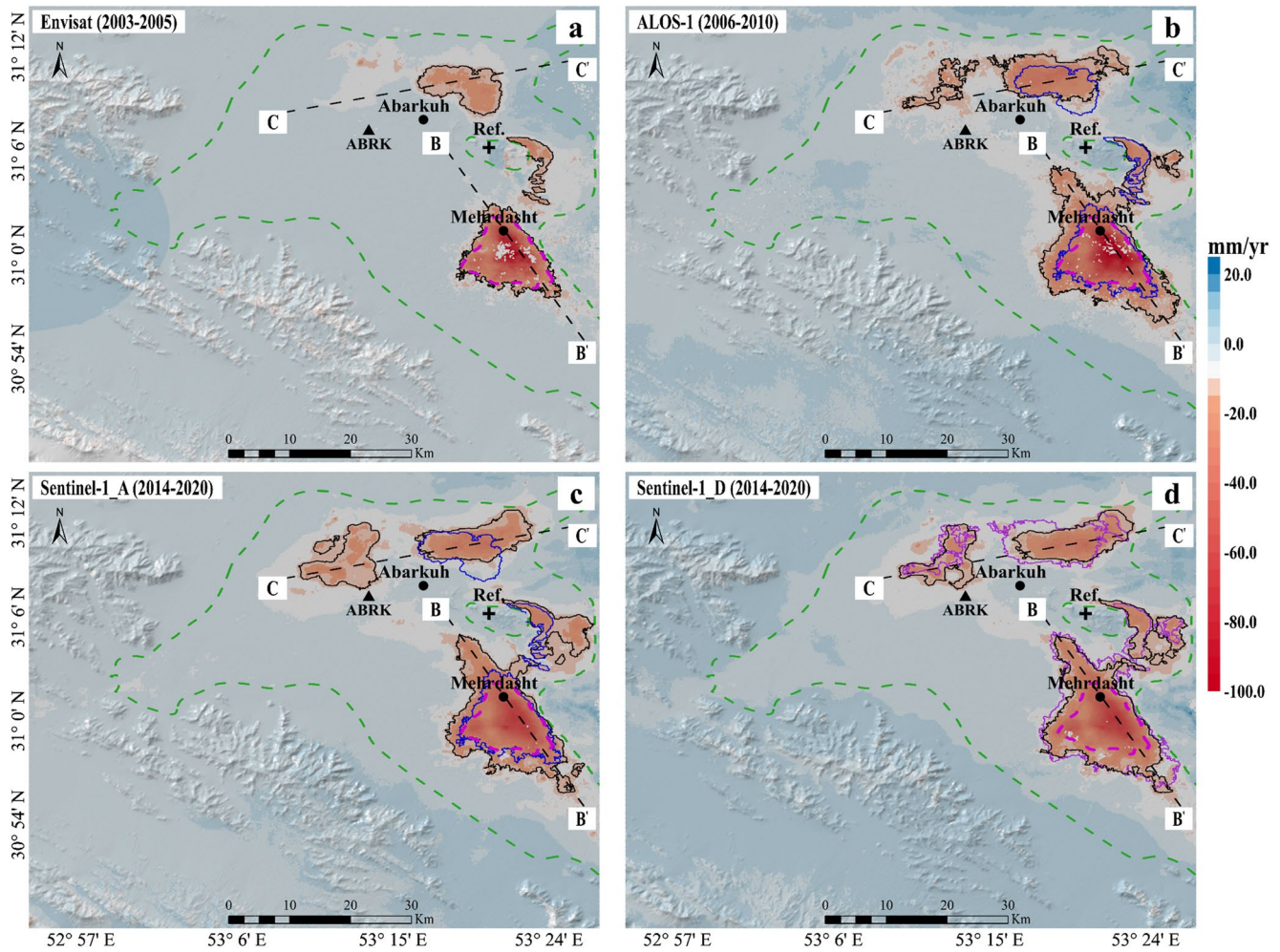


Figure 3. Annual mean vertical velocity maps, derived from the (a) Envisat, (b) ALOS-1, and (c, d) Sentinel-1 ascending and descending data sets, respectively. Red colors show zones of subsidence and white to light-blue colors show areas with little or no displacement. Black circles indicate the major cities, and black dashed lines display the positions of the two profiles ($B-B'$) and ($C-C'$) shown in Figure 4. The green dashed-line polygon in (a–d) shows the Abarkuh Plain aquifer boundary (see Figure 1). Black contours indicate the extent of subsiding areas with a rate of ≥ 12 mm/yr in each data set. Pink dashed lines highlight the Envisat boundary of Main Subsidence Zone. Blue contours in (b, c) and purple contours in (d) mark the extent of the Envisat and ALOS-1 subsiding areas overlaying the ALOS-1 and Sentinel-1 observations. The cross (Ref.) marks the reference pixel located in a stable area. The black triangle in (a–d) shows the location of the ABRK Global Navigation Satellite System station.

Network-Flow Algorithm for Phase Unwrapping (SNAPHU; C. Chen & Zebker, 2003) for phase unwrapping step. We apply mean spatial coherence thresholds of 0.7 and 0.8 to exclude outliers (Figure 2) caused by unwrapping error for the Envisat descending and ALOS-1 ascending data sets, respectively (Tizzani et al., 2007). We use Python based Atmospheric Phase Screen (PyAPS) (Jolivet et al., 2011, 2014) and ERA-5 weather model with spatial resolution of 31 km (Hersbach et al., 2020) to decrease the tropospheric phase. We remove long-wavelength signals in the form of a linear ramp to mitigate the orbital and ionospheric artifacts. For the Envisat data, we correct the Local Oscillator Drift and improve the geo-location accuracy of Envisat interferograms using the empirical model of Marinkovic and Larsen (2013). Finally, all data sets are referenced to a single stable point that presents a coherence value ≥ 0.85 in all data sets (see Figure S6 in Supporting Information S1; cross in Figure 3; Pepe and Lanari, 2006).

We combine the Sentinel-1 descending and ascending time series to calculate the vertical and east-west deformation, supposing no contribution from the north-south component (Wright et al., 2004), through minimizing as:

$$\begin{bmatrix} r_A \\ r_D \end{bmatrix} = V \cdot \begin{bmatrix} v_u \\ v_e \end{bmatrix} - R_{LOS} \quad (1)$$

where (r_A, r_D) are the observation residuals; $v = (v_u, v_e)^T$ is 2D deformation vector (vertical, east-west), and $V = \begin{bmatrix} \cos(\theta_A) & \sin(\theta_A) \cdot \cos(\varnothing_A) \\ \cos(\theta_D) & \sin(\theta_D) \cdot \cos(\varnothing_D) \end{bmatrix}$ is a matrix that includes the Line-Of-Sight (LOS) vectors, where θ and \varnothing are the incidence angle for each Distributed Scatterer (DS) and satellite-heading angle for each orbit, respectively. R_{LOS} contains the LOS observations for the descending and ascending orbits. If Σ_R represents the covariance matrix for errors in the LOS observations, the deformation vector $v = -(V^T \cdot \Sigma_R^{-1} \cdot V)^{-1} \cdot V^T \cdot \Sigma_R^{-1} \cdot R$ can be calculated with a weighted least-squares inversion by minimizing the observation residuals. If the covariance matrix for the vector components is $\Sigma_v = (V^T \cdot \Sigma_R^{-1} \cdot V)^{-1}$ and, as errors in the LOS observations are independent in the descending and ascending measurements, we get

$$\Sigma_v = \sigma^2 (V^T \cdot V)^{-1} \quad (2)$$

where $\sigma^2 = \begin{bmatrix} \sigma_A^2 & 0 \\ 0 & \sigma_D^2 \end{bmatrix}$; and σ_D^2 and σ_A^2 are the standard deviations of descending and ascending orbits, respectively. The square root of diagonal terms of Σ_v gives a standard displacement error that can be used as spatial uncertainties.

As confirmed with the Sentinel-1 descending and ascending data (Figure S7 in Supporting Information S1), we observe minimal contributions of horizontal motions to LOS deformations and convert the LOS velocity maps of the Envisat descending, ALOS-1 ascending, and Sentinel-1 descending and ascending data sets (Figure S8 in Supporting Information S1) to vertical motions using the mean incidence angle value θ of each satellite. In addition, we convert the LOS velocity standard deviation maps (Std_{LOS}), generated through the MintPy time series processing, into maps of the vertical deformation standard deviation ($\text{Std}_v = \frac{\text{Std}_{\text{LOS}}}{\cos\theta}$) (Figure S9 in Supporting Information S1). Temporal uncertainties are calculated by averaging a window of 13×13 pixels at the reference point for each time series epoch for the Envisat, ALOS-1, and Sentinel-1 data sets (Figure S10 in Supporting Information S1; Mirzadeh et al., 2021).

3.2.2. Transition of Elastic to Inelastic Deformation With InSAR-ICA

ICA is a statistical signal decomposition method that expresses random sources as a linear mixture of independent sources that follow a non-Gaussian probability distribution function. The ICA can solve the blind source separation problem by maximizing the statistical independence of independent components (ICs) to separate mixed signal into a number of ICs with distinct temporal (eigenvectors) and spatial (score maps) patterns (Hyvärinen & Oja, 1997). However, a particular process does not certainly associate to a single component as it can contain multiple spatiotemporal patterns divided into several components.

We propose an ICA-based approach to constrain (a) the hydrogeological controls on the spatiotemporal changes in deformation, and (b) the transition from elastic to inelastic deformation in the AP. First, we resample the vertical time series of deformation derived from all data sets into 90m grids and extract 254,550 samples per epoch and 12, 14, 114, and 129 epochs for the Envisat descending, ALOS-1 ascending and Sentinel-1 descending and ascending data sets, respectively. These data are the input to the ICA in the form of a two-dimensional matrix for each data set with size of number of epochs \times number of samples. We use fixed-point algorithm, FastICA (Hyvärinen & Oja, 1997) to solve the ICA. Results for each IC are (a) temporal eigenvectors to present the signal magnitude at each epoch and (b) a score map scaled by the contribution of retained ICs to the mixed signal, showing the pixels that are experiencing the observed temporal eigenvectors. To visually compare the ICs from all data sets, the score maps are standardized to a $[-5, 5]$ range (Figure S11 in Supporting Information S1).

To determine the number of the ICs to retain, we use a Principal Component Analysis (PCA) and the truncation-of-the-variance-explained rule (Cattell, 1966; Jackson, 1993). Too many ICs lead to dividing the components of interest into several “fake” ICs, while too few ICs introduce errors and noise mixing into the components of interest. In contrast to the ICA, the PCA does not require setting a number of components to retain but the variance explained by each component is used to determine the PC's significance. However, the PCA is limited by the forced orthogonality between components, which biases the interpretation of PCs in terms of physical processes. Here, we only use a PCA to identify the number of components explaining a high variance

of the original signal, then we use this number of PCs as the maximum number of ICs to extract. This approach enables bypassing the individual weakness of PCA (forced orthogonality of retrieved components) and ICA (unknown significance of the component to the mixed signal). Based on the PCA results (Table S5 in Supporting Information S2), a single Principal Component (PC) explains 94.6%, 92.8%, 97.2%, and 94.9% of the variance for the Envisat descending, ALOS-1 ascending, and Sentinel-1 descending and ascending data sets, respectively. To explain over 98% of the data variance and to explore the possibility of a secondary signal being “hidden” by the long term deformation captured by the first component, we consider first-four components. Four components explain 98.9%, 98.3%, 98.6%, and 97.3% of the variance in the Envisat descending, ALOS ascending, and Sentinel-1 descending and ascending data sets, respectively (Table S5 in Supporting Information S2 and Figure S11 in Supporting Information S1).

Second, we use the 2-sigma spatiotemporal uncertainties of InSAR results ($2 \times$ maximum of the spatiotemporal uncertainties, giving 95% confidence; see Section 3.2.1) as the threshold to extract the spatial extent of significant surface deformation. This threshold is then converted from millimeters per year (mm/yr) to eigenvectors per year (eig/yr) for each data set:

$$\text{threshold}_m^{\text{eig/yr}} = \frac{\text{threshold}^{\text{cm/yr}}}{\text{Scaled_Score}_m} \quad (3)$$

where Scaled_Score_m is a maximum score scaled with % eigenvectors explained by the dominant IC for data set m . These thresholds are used to mask the score maps to facilitate the identification of the area affected by deformation through time (i.e., the score values lower than the converted thresholds are masked out).

3.2.3. Least Squares-Based Time Series Decomposition

We use a model for the temporal evolution of deformation to estimate the linear trend and average periodic amplitude (Goudarzi et al., 2015):

$$Y(t_i) = a + b \times t_i + c \times \sin(2\pi \times t_i) + d \times \cos(2\pi \times t_i) + e \times \sin(4\pi \times t_i) + f \times \cos(4\pi \times t_i) \quad (4)$$

where t_i ($i = 1, 2, \dots, N$) are the time steps of the time series; a and b are offset and linear slope, respectively, and (c, d) and (e, f) are the annual and seasonal scales for sine and cosine functions, respectively. By considering the unknown coefficients as a vector $X = [abcdef]^T$, the equation can be written for all time steps in a matrix form and solved using least squares method to isolate the nonlinear (seasonal) and linear (long-term) components of time series. We apply this approach to the GNSS and InSAR-derived time series of land deformation to derive the linear and seasonal components, as well as to assess the dominant IC.

4. Results and Analysis

4.1. Spatial-Temporal Patterns and Rates of Deformation

The multi-sensor analysis of deformation in the AP allows us to see the temporal changes in the patterns and rates of deformation. Figure 3 shows the mean vertical velocity maps converted from the mean LOS velocities (Figure S8 in Supporting Information S1), and reveals three major subsidence features in the AP. In terms of subsidence rates, the most substantial feature is a northwest-southeast elongated zone referred to as the Main Subsidence Zone (MSZ) that covers an initial area of 37.4 km² with a rate ≥ 12 mm/yr (three-sigma maximum spatiotemporal uncertainties; Figures S9 and S10 in Supporting Information S1) in the Envisat period (2003–2005). The MSZ spatially expanded between the Envisat, ALOS-1 (2006–2010), and Sentinel-1 (2015–2020) data sets and reaches 135 km² in the Sentinel-1 descending and ascending data set. In addition to the MSZ, a new deformation region appears in the ALOS-1 and Sentinel-1 data sets northwest of the Abarkuh city (black circle in Figures 3b–3d) with a subsidence rate of 13 mm/yr. The profile $B-B'$ (Figure 4, map location shown in Figure 3) highlights the expansion of the MSZ toward the northwest between 2 and 8 km in both the Sentinel-1 and ALOS-1 data sets compared to the Envisat data (shaded area in Figure 4a). In the center of the MSZ, we detect an increase followed by a decrease in the subsidence rates by 30 and 40 mm/yr, respectively, between 9.5 and 15 km (shaded area in Figure 4a). Hydrogeological data reveal a direct correlation between this deformation and the average rate of head level changes: head levels decline accelerated by ~ 0.18 m/yr in the

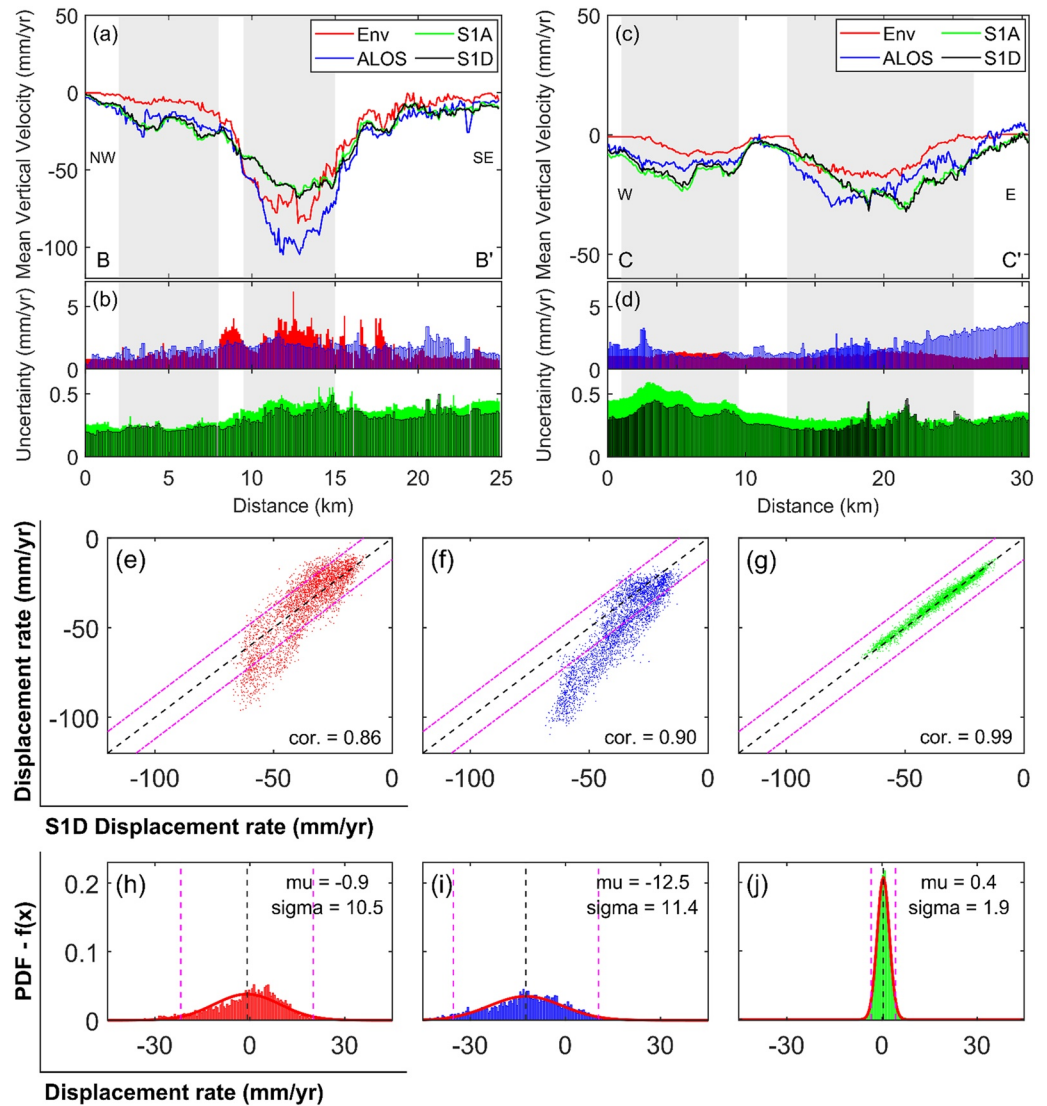


Figure 4. Annual mean vertical velocities and sigma uncertainties derived from the Envisat (red), ALOS-1 (blue) and Sentinel-1 descending (black) and ascending (green) data sets along ($B-B'$) (a and b) and ($C-C'$) (c and d) profiles (profile lines shown in Figure 3). The shaded parts highlight the locations of considerably different subsidence rates in the Envisat, ALOS-1, and Sentinel-1 descending and ascending data sets. Lateral expansion of the subsiding areas is visible along both profiles. (e–g) Comparisons of the annual mean vertical velocities derived for resampled common points in a 90 m grid within the Main Subsidence Zone (MSZ) (pink dashed-lines in Figure 3a). The Sentinel-1 descending annual mean vertical velocity is used as the reference (shown on x -axis) and compared to the (e) Envisat, (f) ALOS-1, and (g) Sentinel-1 ascending data sets. The dashed black and dashed-dotted pink lines in (e–g) show the identical vertical displacement rates and a 3-sigma range of ± 12 mm/yr, respectively. (e–g) indicate that the subsidence rates from the Envisat, ALOS-1, and Sentinel-1 ascending data sets are highly correlated with the Sentinel-1 descending data set. (h–j) probability density function of differential annual mean vertical velocities derived for the resampled common points between the Sentinel-1 descending annual mean vertical velocity as the reference and (h) Envisat, (i) ALOS-1 and (j) Sentinel-1 ascending data sets. The dashed black and pink lines in (h–j) show the mean and 2-sigma values for the data sets. Both (g and j) also confirm that there is no significant horizontal deformation captured in the Sentinel-1 data set within the MSZ.

MSZ between the Envisat and ALOS-1 data sets, while the average rate of head decline decreased by ~ 0.26 m/yr between the ALOS-1 and Sentinel-1 data sets (Figures S4f–S4h in Supporting Information S1). Further changes in the extent and rates of deformation in north of Abarkuh city along the profile $C-C'$ are shown in Figure 4c. The observed deformation is consistent with an increased rate of head decline northwest and north of the AP aquifer between the Envisat, ALOS-1, and Sentinel-1 data sets (dark green areas in Figures S4d and S4e in Supporting Information S1).

Figure S5 in Supporting Information S1 shows the time series of vertical, north-south, and east-west displacements from the daily GNSS data of the ABRK permanent GNSS station (see Figure 3 for location), and reveals subsidence of 2.9 mm/yr before July 2011 that increased to 5.6 mm/yr after July 2011 (red and blue dashed lines in Figure S5a in Supporting Information S1). In addition, Figures S5c and S5e in Supporting Information S1 reveal displacement rate of more than 22 mm/yr in the north-south and east-west components possibly caused by an accommodation for shortening of the Arabian-Eurasian collision zone (Djamour et al., 2011; Khorrami et al., 2019).

4.2. Uncertainties and Consistency Assessment

We explore the uncertainties and consistency of mean vertical velocities from the Envisat, ALOS-1, and Sentinel-1 ascending and descending data sets. Figure S9 in Supporting Information S1 shows that the uncertainties of velocities are mostly less than 4 mm/yr over the study area. Mean deformation rate uncertainties along profiles are shown in Figures 4b and 4d. The Sentinel-1 data sets have the smallest mean uncertainties: 0.3 mm/yr for both ascending and descending. The ALOS-1 and Envisat data sets have mean uncertainties of about 1 and 2 mm/yr along the profiles $C-C'$ and $B-B'$, respectively (see Figure S9 in Supporting Information S1 for maps of estimated sigma uncertainties). Figure S10 in Supporting Information S1 shows that the majority of epochs have vertical position uncertainties <2 mm in all data sets, with exception of three epochs (Figures S10b and S10c in Supporting Information S1), likely contaminated by atmospheric turbulences (Yunjun et al., 2019).

We compare the mean vertical velocities derived from the four time series for resampled common points in a 90 m grid within the MSZ (pink dashed-lines in Figure 3a), with the Sentinel-1 descending data being used as the reference (Figures 4e–4g). Moreover, we explore the probability density function (PDF) of differential mean vertical velocities between the Sentinel-1 descending data and other data sets for these resampled common points (Figures 4h–4j). Correlation coefficients between the mean velocities of Sentinel-1 descending data and the other data sets range between 0.86 and 0.99, indicating strong consistency. The average differential velocities of 0.4 ± 1.9 mm/yr (Figure 4j) and the agreement between Sentinel-1 descending and ascending data sets (Figure 4g) support the assumption of no significant horizontal motion within the MSZ (more detail shown in Figure S7 in Supporting Information S1). The Envisat data displays the lowest correlation with the Sentinel-1 descending data (0.86), likely due to spatiotemporal changes in the subsidence rates, and the average differential velocities of 0.9 ± 10.5 mm/yr also suggest that changes in deformation rates exist. The ALOS-1 data has a good agreement (0.90) with the Sentinel-1 descending data, but Figures 4f and 4i shows that the subsidence rate decreased by a mean of 12.5 mm/yr within the MSZ.

We compare the InSAR deformation time series derived from the ALOS-1 ascending and Sentinel-1 descending and ascending data sets with daily GNSS data from the ABRK permanent station for overlapping time-spans. Figure S5a in Supporting Information S1 shows a good consistency between the subsidence rates from the Sentinel-1 ascending and descending data set (4.7 and 5.0 mm/yr) and GNSS data (5.6 mm/yr) between 2014 and 2020. However, the subsidence rate from the ALOS-1 data (5.5 mm/yr) is greater than that from the GNSS data (2.9 mm/yr) during 2007–2011. This discrepancy is less than the estimated maximum spatiotemporal uncertainties of the ALOS-1 data (Figures S9b and S10c in Supporting Information S1) and could not be attributed to the InSAR processing errors or difference in the scale of the InSAR pixel and GNSS footprint.

4.3. Controls on Temporal Changes of Inelastic Compaction

Groundwater pumping lowers water levels and decreases pore water pressure in an aquifer system, in turn, increasing the effective stress. Once the hydraulic head drops below the previous lowest level, inelastic deformation happens due to permanently collapsing pore spaces, especially in the fine-grained aquitards which are more prone to the inelastic deformation than coarse-grained aquifer layers (Meade, 1964; Wilson & Gorelick, 1996). Since pumping rates are inhomogeneous in space and time and sediment properties vary spatially, the elastic and inelastic contributions to the observed deformation can change spatially over time. To assess the spatiotemporal changes of inelastic and elastic deformations, we apply the ICA to the time series derived from the Envisat, ALOS-1, and Sentinel-1 descending and ascending data sets (Figure S11 in Supporting Information S1).

The first component (IC1) displays a spatial pattern similar to the mean deformation rate maps of all data sets (Figure 3; Figure S11 in Supporting Information S1). Each temporal eigenvector shows nearly linear trend with

slopes of -0.55 , -0.85 , -0.61 , and -0.65 eigenvectors/yr (-91.2 , -102.2 , -64.2 , and -66.7 mm/yr) for the Envisat, ALOS-1, and Sentinel-1 ascending and descending data sets, respectively (Figures 5e–5h; Figure S11 in Supporting Information S1). IC2 shows positive score values limited to the northeast of the MSZ for the ALOS-1 data (Figure S11b in Supporting Information S1) and a noisy signal (mix of positive and negative scores) within the MSZ for the Envisat data (Figure S11a in Supporting Information S1). IC2 has temporal eigenvectors with the slight descending slopes of -0.01 , -0.09 , -0.09 , and -0.18 (in eigenvectors/yr) for the Envisat, ALOS-1, and Sentinel-1 ascending and descending data sets, respectively. IC3 shows no clear pattern in the score maps for the ALOS-1, and Sentinel-1 ascending and descending data sets, but has positive score values north of the MSZ in the Envisat data, with a temporal eigenvector slope of -0.22 (in eigenvectors/yr). IC4 score map shows a correlated zone in the northeastern zone of subsidence in the Envisat and ALOS-1 data sets and in the northwestern zone of the land subsidence in the Sentinel-1 ascending and descending data set with temporal eigenvectors with the slight downward trends with slopes of -0.16 , -0.07 , -0.18 , and -0.07 eig/yr for the Envisat, ALOS-1, and Sentinel-1 ascending and descending data sets, respectively.

Based on the temporal eigenvectors showing a linear signal and the score map pattern being consistent with the spatial pattern of the mean vertical deformation rate map (Figure 3; Figure S11 in Supporting Information S1), we consider that the IC1 highlights inelastic deformation, associated with severe aquifer storage depletion with a roughly linear head decline since 1984 (Figure S12a in Supporting Information S1). This assumption is backed up by observations of a roughly linear declining trend in (a) hydraulic head in most piezometers (Figure S2 in Supporting Information S1) and (b) aquifer storage values (Figure S12 in Supporting Information S1). The linear trend in long-term deformation may arise from the fact that the aquitards (mostly clay units) in the AP are very thick (up to 180 m thickness in P5 shown in Figure S1 in Supporting Information S1) in comparison with the aquifer units (gravel and sand). Having a continuing severe storage depletion along with the presence of the thick aquitards in the AP, the roughly linear land deformation behavior may theoretically last for a long time up to the future (years or decades (Ireland et al., 1984)). In addition, having a roughly linear decline trend in both the head and deformation time series (Figures 5g and 5h; Figure S2 in Supporting Information S1), we assumed that a semi-equilibrium condition has occurred between the inelastic compaction and long-term change in the head, which has also been made for the Las Vegas Valley (Bell et al., 2008) and the Gorgan plain (Rezaei et al., 2020; Rezaei & Mousavi, 2019) to estimate the inelastic aquifer properties. Smith and Li (2021) also noted that inelastic deformation has an overall negative trend, whereas the elastic deformation is primarily seasonal with no long-term trend. There is a roughly thick fine-grained units layers (dominantly clay) surrounding the thinner aquifer units (please see wells P1–P4 in Figure S1 in Supporting Information S1). Figure 5 shows the spatiotemporal patterns of IC1 score maps that mostly highlight the evolution of the inelastic deformation. The growth in the spatial extent of IC1 positive score with time is clearly visible around the MSZ and two extra zones to the north between the Envisat and Sentinel-1 periods. The temporal eigenvectors of IC2 component derived from all data sets (Figures 5e–5h; Figure S11 in Supporting Information S1) display no clear elastic deformation during the study period, suggesting that inelastic deformation dominates. The results of temporal eigenvectors show that the rate of IC1 component decreases between the Envisat and Sentinel-1 data sets observation periods, with a peak occurring during the 2006–2010 period imaged by the ALOS-1 data (Figures 5e–5h). This is consistent with the head changes between the Envisat, ALOS-1, and Sentinel-1 periods within the MSZ (Figures S4f–S4h in Supporting Information S1), where the head decline experienced a rate increase followed by a rate decrease, confirming the inelastic deformation pattern extracted by the ICA.

In addition to this inelastic signal, a small portion of the deformation in the AP may be the elastic as suggested by the seasonal component of vertical deformation of GNSS data observed in Figure S5b in Supporting Information S1 (Hoffmann et al., 2001; Rezaei et al., 2020; Riley, 1969; Smith & Li, 2021). However, no such seasonal signal has specially been captured by a single component. Instead, IC2–IC4 are dominated by the long-wavelength signals with the low-amplitude eigenvectors more likely to be reflecting orbital errors and atmospheric delay rather than subsidence. Despite the dry conditions, a seasonal signal of small magnitude is observed in part of the IC1 temporal eigenvectors of the Sentinel-1 ascending and descending data set (Figures 5g and 5h). This mixing within the long-term deformation emphasizes the variability and minimal contribution of this seasonal signal to the full deformation (see Section 5.1 for further discussion). Smith and Li (2021) suggested that inelastic deformation can follow a seasonally variable trend. Hence, this observed seasonality in IC1 could relate either to elastic or inelastic deformation. As the inelastic compaction lags behind water level fluctuations, the tempo-

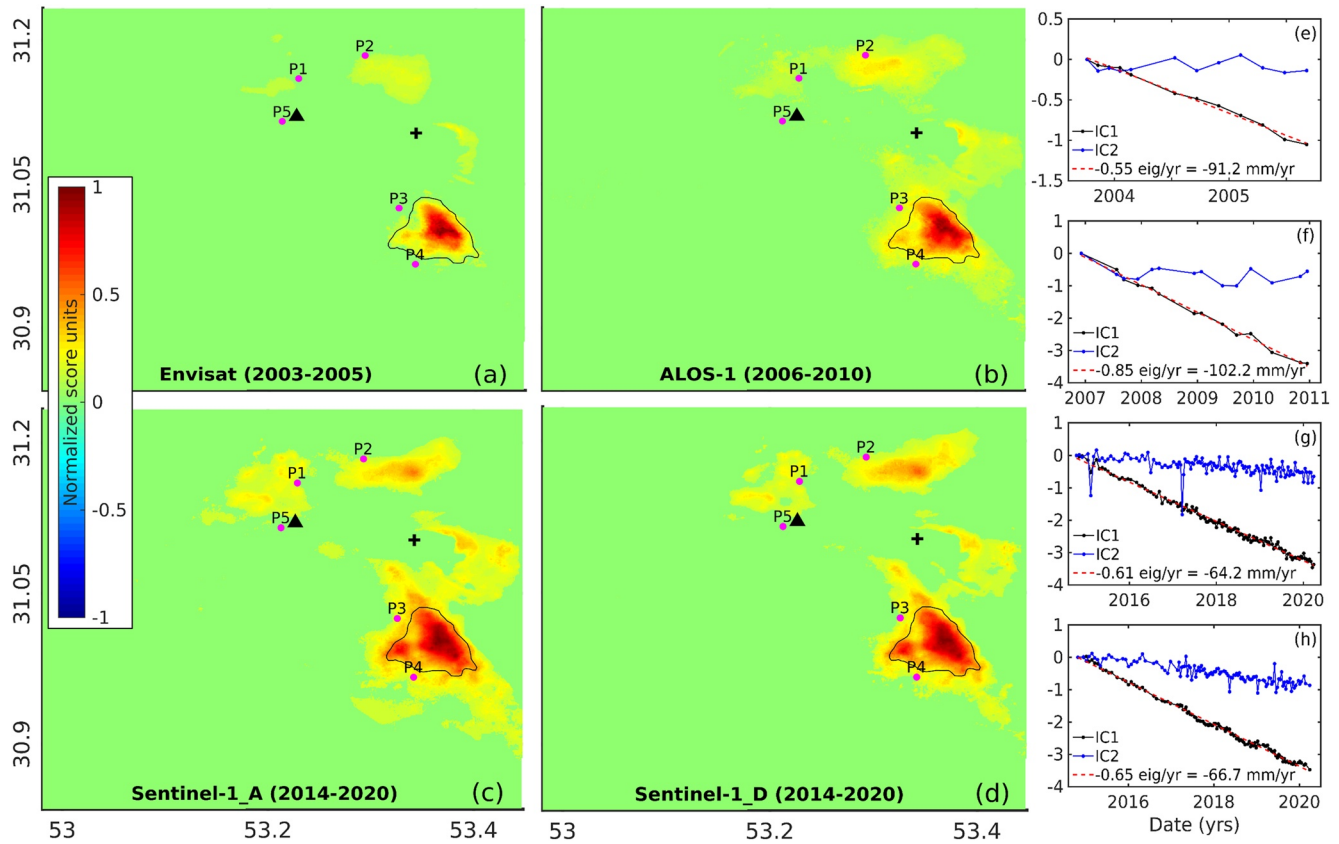


Figure 5. (a–d) Score maps of IC1 component derived from the (a) Envisat, (b) ALOS-1, and (c and d) Sentinel-1 ascending and descending time series of inferred vertical motions. The cross marks the reference point placed in the stable area. The black polygon shows the boundary of the Main Subsidence Zone. Pink circles show the locations of the exploration wells (data shown in Figure S1 in Supporting Information S1). (e–h) Temporal Eigenvectors of IC2 (blue) and IC1 (black) components, derived from the (e) Envisat, (f) ALOS-1, and (g–h) Sentinel-1 ascending and descending data sets (see details of ICs1-4 in Figure S11 in Supporting Information S1). The red dash lines show the best-fit linear regression of the IC1. The black triangle in (a–d) shows the location of the ABRK Global Navigation Satellite System station.

ral variability of the seasonal signal could help isolate its source when considered together with lithologic and hydrologic data (Section 5).

To investigate the initiation and controls on the inelastic deformation, we combine the score maps of the IC1 components (Figures 5a–5d) with the spatiotemporal patterns of head changes (Figure S3 in Supporting Information S1) and lithological data from five exploration wells (Figure S1 in Supporting Information S1, see the locations in Figure 6a). Figure 6a shows the overlap of IC1 score maps from all data sets. Red colors highlight areas of long-term inelastic deformation during all three observation periods. Light-blue colors indicate the growth in the extent of the inelastic deformation extents captured by the Envisat to ALOS-1 transition, referred to as Expansion(A). Dark blue colors demonstrate the expansion of inelastic deformation zone between the ALOS-1 and Sentinel-1 periods, referred to as Expansion(S). Figures 6b–6e show the annual head changes (m/yr) for the periods of the Envisat, ALOS-1 and Sentinel-1 data sets, as well as for the full 2003–2019 period, respectively. Figures 6f and 6g show the differential maps of annual head changes (m/yr) between the Envisat and ALOS-1 periods, and the ALOS-1 and Sentinel-1 periods, respectively. We see that, with time, the inelastic deformation has expanded to areas outside of the MSZ to the north of AP, correlated with hydraulic head declines. The maximum expansion in inelastic deformation is Expansion(A) (light blue in Figure 6a) with 119 km². The zone of long-term inelastic deformation common to all data sets (red in Figure 6a) and the Expansion(S) (dark-blue in Figure 6a) are estimated to be 90.4 and 24.2 km², respectively. Figure 6e confirms that the MSZ and its surrounding areas have the highest long-term rate of head decline. By combining the hydraulic data with lithologic data (Figure 6e; Figure S1 in Supporting Information S1), we observe that the head decline involves mostly fine-grained sediments for example, clay-rich unit layers. The increase in effective stress caused by such head decline likely triggered the compaction of the clay layers and resulting inelastic deformation.

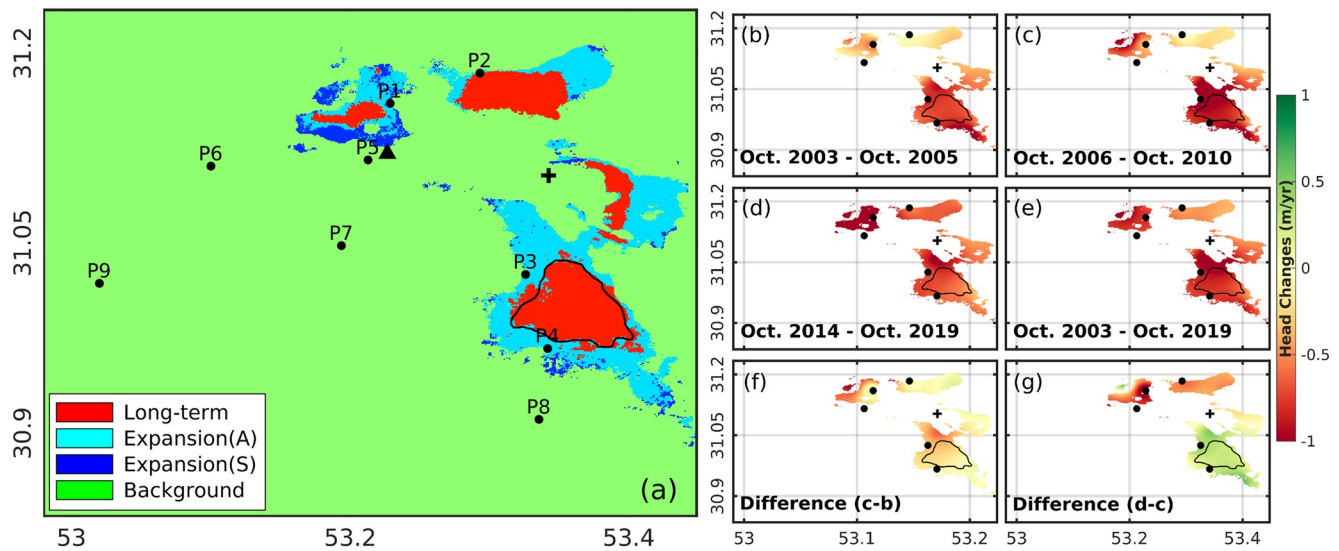


Figure 6. (a) Spatial extent of inelastic deformation in the Abarkuh Plain from the Envisat, ALOS-1, and Sentinel-1 ascending and descending data sets. Red color displays areas of long-term inelastic deformation in common between the four data sets. Light-blue and dark-blue colors show areas associated with the Expansion(A) (Envisat to ALOS-1) and Expansion(S) (ALOS-1 to Sentinel-1), respectively. (b–e) Interpolated maps of the annual head changes for the periods of the (b) Envisat, (c) ALOS-1, (d) Sentinel-1 data sets, and (e) 2003–2019, masked to show the areas experiencing inelastic deformation. (f–g) Interpolated differential annual head change between the (f) Envisat and ALOS-1 periods and the (g) ALOS-1 and Sentinel-1 periods. The cross shows the reference point in a stable area. Black circles show the locations of exploration wells (shown in Figure S1 in Supporting Information S1). The black polygon indicates the boundary of the Main Subsidence Zone. The black triangle in (a) shows the location of the ABRK Global Navigation Satellite System station.

Figure 6f shows that the water heads mostly declined in the MSZ and its surrounding areas between the Envisat and ALOS-1 periods, suggesting that this decline caused inelastic deformation expansion (Expansion(A), light-blue in Figure 6a) as extents experiencing elastic deformation can transition to experiencing the inelastic deformation once stress exceeds the preconsolidation stress (Ireland et al., 1984). In contrast, in most cases, the transition from the inelastic to purely elastic deformation cannot occur in a short time period (Ireland et al., 1984), explaining that the decrease in the rate of water head lowering during the ALOS-1 to Sentinel-1 transition in the MSZ did not coincide with a reduction of the area experiencing the inelastic deformation. A similar correlation between the timing of expansion of the area experiencing inelastic deformation and water heads change is observed in the northwest of the AP. There, Expansion(S) dominates, which is consistent with the hydraulic heads declining between the ALOS-1 and Sentinel-1 periods.

5. Drivers and Discussion

5.1. Outline of the Confined Aquifer

Confined aquifers usually have much larger seasonal fluctuations in hydraulic head levels than unconfined aquifers, which drives the seasonal change in effective stress and deformation. In confined aquifers, seasonal deformation is mostly controlled by the compressibility changes of the sediment's skeletal matrix in response to seasonal hydraulic head fluctuations or seasonal recharge. In contrast, in unconfined aquifers, water volume fluctuations in the pore spaces is the dominant driver of storage variation (Rezaei, 2018), which induce only little deformation. Thus, deformation can be used to outline the spatial extent of confined aquifers, as previously done in the Gorgan and Salmas plains in northern Iran (Rezaei & Mousavi, 2019; Shahbazi et al., 2022). In the AP, a slight seasonality in the IC1 temporal eigenvectors of the Sentinel-1 descending and ascending data sets (Figures 5g and 5h), suggests a modest response to the seasonal fluctuations in pumping rates of wells (see Figure S12b in Supporting Information S1 for a plot displaying the seasonal signals in monthly storage variations), mixed with the dominant long-term inelastic deformation (Figure 6a). In addition, the vertical deformation time series from the GNSS station clearly shows seasonality, the amplitude of which seems to have increased since July 2011 (Figure S5b in Supporting Information S1). These observations suggest that the geodetic data capture the sum of the deformation processes occurring from the surface to stable substrate at a given location, and elastic deformation may concurrently happen in coarse-grained aquifer units while the inelastic deformation occurs

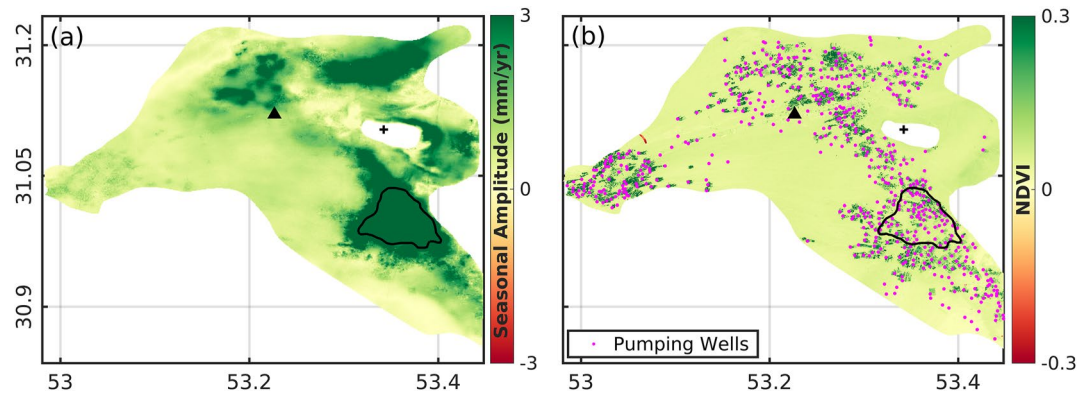


Figure 7. (a) Map of seasonal amplitude of vertical deformation from the Sentinel-1 descending data that highlights the boundary of confined aquifer. This seasonal amplitude map is mapped using the variation of each pixel between the dry and wet seasons through removing the inelastic component of land deformation. (b) Average Normalized Difference Vegetation Index in the 2019–2020 hydrological year across the Abarkuh Plain aquifer using the Sentinel-2 data. The black polygon shows the boundary of Main Subsidence Zone. The cross and black triangle show the reference pixel in a stable area and the location of ABRK Global Navigation Satellite System station, respectively. The pink dots in (b) display the pumping wells' locations.

in fine-grained units (see gravel and sands sediments interbedded with thick clay layers at P1 in Figure 1). We further map the boundary of the seasonal vertical displacement across the AP aquifer (Figure 7a) using the IC1 temporal eigenvector of the Sentinel-1 descending data (see Section 3.2.2 for the detail of data used), after removing the linear long-term (inelastic) displacement. Figure 7a shows that the extent of the seasonal deformation with an amplitude ≥ 3 mm/yr coincides with the extent of the long-term inelastic deformation (Figure 5d) where the exploration wells (e.g., P1 in Figure S1a in Supporting Information S1) show presence of the coarse-grained unit layers interbedded by the thick fine-grained aquitards. We interpret this seasonal deformation extent as marking the boundary of the confined aquifer in which most pumping wells are positioned (Figure 7b) (Rezaei & Mousavi, 2019; Shahbazi et al., 2022). This confined aquifer appears to extend deeper than 215 m, where the coarse-grained gravel and sand units are located underneath a thick (~ 183 m) fine-grained clay and silt unit. This interpretation is supported by observations that the groundwater has risen above the top of aquifer at some of the exploration wells just after drilling termination, which is the typical behavior of confined aquifers. For example, a water rise of 22 m can be seen at P5 at the end of drilling process of exploration well (Figure S1e in Supporting Information S1). Notably, the maximum seasonal signal amplitude in the AP is smaller than those observed in the Gorgan (~ 50 mm/yr) and Salmas (~ 120 mm/yr) plains, most due to that the annual recharge (in turn, annual rebound) is less in the AP with highly drier climate (average annual rainfall of ~ 86 mm/yr) than the Gorgan (244–800 mm/yr) and Salmas (~ 264 mm/yr) plains, with wetter climates. However, we captured such small seasonal amplitude across the AP using ICA but not in a single component, signifying the usefulness of the ICA for land deformation investigation.

These observations suggest that even with the inelastic deformation dominating, the aquifer system still reacts to fluctuating seasonally-driven pumping rates or varying recharge components (Table S1 in Supporting Information S2). When the head in fine-grained and clay-rich units is above the preconsolidation head, these units deform elastically together with the coarse-grained unit. In contrast, when the head in fine-grained and clay-rich units is below the preconsolidation head, these units deform inelastically while coarse-grained units deform elastically.

5.2. Drivers of Inelastic Compaction

Groundwater observations in the aquifer system over 33 years (1984–2016) (Figure S12a in Supporting Information S1) reveal a mean water level drop of 20 m associated with $\sim 1,147$ million cubic meters (MCM) of the storage loss (Iran's WRM Co., 2014). Where clay layers are present, such as massive drop in water levels is likely to cause the stress exceeding the preconsolidation stress, triggering the observed irreversible subsidence. Lithologic data at P1–P4 shows clay thicknesses exceeding 70 m, hinting at a direct correlation between the occurrence of inelastic deformation and the subsurface lithology in areas experiencing dropping the water heads. In contrast, lithologic data at P6–P9 where no significant subsidence is observed (less than 1 mm/yr) while water heads

are dropping, reveal thick coarse-grained sediments (Figures S1f–S1i in Supporting Information S1), further confirming that the subsidence is correlated with clay thicknesses.

Differential maps of the annual head changes across the area experiencing the inelastic deformation show a continuous decline in head levels during 2003–2019, with an acceleration in the rate of head decline during the ALOS-1 observation period. This rapid head decline resulted in the most substantial growth of areas affected by the inelastic deformation. This transition to the inelastic deformation is well captured by our multi-temporal InSAR-ICA approach and highlights the timing during which hydraulic heads reach a new low, which initiated the inelastic deformation driven by the stress in the clay unit layers exceeding the pre-consolidation stress. These results are similar to those documented in the Salmas Plain, Iran (Shahbazi et al., 2022), San Joaquin Valley, California (Smith et al., 2017), and San Luis Valley, Colorado, USA (Chen et al., 2016) where the link between an acceleration in the depletion of aquifer storage and inelastic subsidence driven by compaction of fine-grained units was shown.

5.3. Uncertainties

It is important to note that there are uncertainties associated with the InSAR results and with separation of inelastic and elastic components of deformation that influence the assessment of aquifer properties.

First, tropospheric noise that biases the InSAR deformation field, is evident in the Envisat data (Figure 3a), when comparing the Envisat mean velocity map to those from the ALOS-1 and Sentinel-1 data sets likely due to the limited number of Envisat acquisitions. In addition, while we document minimal horizontal displacements during the Sentinel-1 period using the ascending and descending orbits, there may have been horizontal motion during the Envisat and ALOS-1 periods, which we could not quantify due to the lack of observations from two independent orbits. Such horizontal deformation would bias the signal decomposition and the resulting vertical deformation. Second, the thickness and extent of aquifers and aquitards layers are poorly resolved in lithological data due to the sparse nature of exploration wells. This causes potential biases when interpolating the lithologic data and then converting the observed deformation to aquifer storage values.

Another source of uncertainty comes from separating the elastic from inelastic components of the displacement in the aquifer system which can affect the calculation of elastic and inelastic skeleton coefficients, and recoverable and irrecoverable groundwater storage loss. The linear trend maps of deformation using least squares method (Figures S13a–S13d in Supporting Information S1) display a good consistency with the dominant component of ICA results (Figure S11 in Supporting Information S1), suggesting that the ICA successfully isolated a nearly linear trend for all data sets. However, we also document an overlap between the IC1 and ICs3-4 in the Envisat data, which is likely associated with the larger noise component of Envisat data. Moreover, seasonality is seen in the IC1 temporal eigenvectors of both Sentinel-1 descending and ascending data sets. The lack of separation of signal into an individual component is likely due to (a) the small amplitude of signal, and (b) overlapping spatial patterns of the seasonal signal with that of the longer-term (see Section 5.1). It is essential to consider such superposition of the signals when estimating the values of recoverable and irrecoverable groundwater storage, as well as elastic and inelastic skeleton coefficients.

6. Conclusions

To develop sustainable aquifer protection plans and assess the impact of current pumping practices, it is critical to quantify the spatially variable initiation of inelastic deformation. We used a 2003–2020 InSAR multi-sensor time series analysis combined with an ICA and hydrogeological data to pinpoint the timing of the transition to inelastic deformation within various parts of the AP aquifer system. Our work highlights (a) the need to revise current pumping practices to defend the groundwater resources in Central Iran, (b) the potential of using InSAR time series to determine the confined aquifer extension as well as evaluate the sustainability of such practices, and (c) the necessity to consider the spatiotemporal correlation of processes causing ground deformation when interpolating InSAR mean velocity maps.

Our data show a northwest-southeast elongated zone of land subsidence in the AP covering a maximum area of ~ 135.1 km² in the Sentinel-1 data (2014–2020). The ICA of the InSAR data set reveals that the majority of long-term observed subsidence (partially recoverable) is inelastic and captured by a single component (IC1), consistent with hydrogeological settings and measurements. We displayed the areas with experiencing inelastic deformation have significantly extended over time as a result of water levels locally reaching new lows that result in clay units

experiencing stress exceeding the pre-consolidation stress. The high temporal sampling of Sentinel-1 data (as low as 6 days) also enables detecting small-magnitude seasonal deformation in region of the confined aquifer system that still reacts to the seasonal fluctuations in groundwater storage, despite extremely dry climate condition with low annual recharge. The observations confirm that elastic deformation may incorporate into inelastic deformation and the observed land deformation is the result of these multiple process occurring simultaneously within different units of subsurface. Therefore, complicating interpretation of the surface deformation data in terms of physical processes when the signal is not decomposed. Our results highlight the significant loss of the underground water resources over the past two decades in the AP and point out that we are near a tipping point between sustainability and substantial damage to the underground water resources in Iran, emphasizing the fact that current decisions have the potential to change natural resources landscape permanently.

Data Availability Statement

The geological and hydrological (i.e., piezometers, logs of exploration wells, and pumping wells), and daily GNSS data are accessible by contacting the Geological Survey and Mineral Explorations of Iran (GSI), Regional Water Company of Yazd, and National Cartography Center of Iran (NCC) respectively. The Envisat and Sentinel-1 data sets are copyrighted by the European Space Agency (ESA) and freely accessible through the ESA archive and Alaska Satellite Facility (ASF) archive. The processed InSAR results, including the time series of deformation and velocity maps, as well as the GNSS and hydrogeological data and geological maps can be accessed in a public repository at the following link (<https://doi.org/10.5281/zenodo.7786511>). The ERA5 and SRTM DEM data are provided through the Copernicus Climate Data Store and NASA's Land Processes Distributed Active Archive Center (LP DAAC), located at USGS Earth Resources Observation and Science (EROS) Center, respectively. InSAR Scientific Computing Environment, Miami INsar Time-series software in PYthon (MintPy), and Python 3 Atmospheric Phase Screen (PyAPS) are available in their pages: <https://github.com/isce-framework/isce2>, <https://github.com/insarlab/MintPy>, and <https://github.com/insarlab/PyAPS>.

Acknowledgments

The Strategic Priority Research Program Project of the Chinese Academy of Sciences (Grant XDA23040100) and the CAS-TWAS President's Fellowship supported this research. The Japan Aerospace Exploration Agency (JAXA) provided ALOS-1 data within RA6 (PI 3059). The authors thank the Regional Water Company of Yazd, Iran's Water Resources Management Company, and Geological Survey & Mineral Exploration of Iran (GSI) for the hydrogeological and geological information of the AP. We also thank the National Cartography Center of Iran (NCC) for providing us with the daily permanent ABRK GNSS data. We thank editors and two anonymous reviewers for their comments that significantly improved the manuscript.

References

- Aimaiti, Y., Yamazaki, F., & Liu, W. (2018). Multi-sensor InSAR analysis of progressive land subsidence over the Coastal City of Urayasu, Japan. *Remote Sensing*, *10*(8), 1304. <https://doi.org/10.3390/rs10081304>
- Bai, L., Jiang, L., Zhao, Y., Li, Z., Cao, G., Zhao, C., et al. (2022). Quantifying the influence of long-term overexploitation on deep groundwater resources across Cangzhou in the North China Plain using InSAR measurements. *Journal of Hydrology*, *605*, 127368. <https://doi.org/10.1016/j.jhydrol.2021.127368>
- Bell, J. W., Amelung, F., Ferretti, A., Bianchi, M., & Novali, F. (2008). Permanent scatterer InSAR reveals seasonal and long-term aquifer-system response to groundwater pumping and artificial recharge. *Water Resources Research*, *44*(2). <https://doi.org/10.1029/2007wr006152>
- Berardino, P., Fornaro, G., Lanari, R., & Sansosti, E. (2002). A new algorithm for surface deformation monitoring based on small baseline differential SAR interferograms. *IEEE Transactions on Geoscience and Remote Sensing*, *40*(11), 2375–2383. <https://doi.org/10.1109/tgrs.2002.803792>
- Bürgmann, R., Rosen, P. A., & Fielding, E. J. (2000). Synthetic aperture radar interferometry to measure Earth's surface topography and its deformation. *Annual Review of Earth and Planetary Sciences*, *28*(1), 169–209. <https://doi.org/10.1146/annurev.earth.28.1.169>
- Calderhead, A. I., Therrien, R., Rivera, A., Martel, R., & Garfias, J. (2011). Simulating pumping-induced regional land subsidence with the use of InSAR and field data in the Toluca Valley, Mexico. *Advances in Water Resources*, *34*(1), 83–97. <https://doi.org/10.1016/j.advwatres.2010.09.017>
- Cattell, R. B. (1966). The scree test for the number of factors. *Multivariate Behavioral Research*, *1*(2), 245–276. https://doi.org/10.1207/s15327906mbr0102_10
- Chang, L., Jin, S. G., & He, X. (2014). Assessment of InSAR atmospheric correction using both MODIS near-infrared and infrared water vapor products. *IEEE Transactions on Geoscience and Remote Sensing*, *52*(9), 5726–5735. <https://doi.org/10.1109/TGRS.2013.2292070>
- Chaussard, E., Bürgmann, R., Shirzaei, M., Fielding, E. J., & Baker, B. (2014). Predictability of hydraulic head changes and characterization of aquifer-system and fault properties from InSAR-derived ground deformation. *Journal of Geophysical Research: Solid Earth*, *119*(8), 6572–6590. <https://doi.org/10.1002/2014jb011266>
- Chaussard, E., Havazli, E., Fattahi, H., Cabral-Cano, E., & Solano-Rojas, D. (2021). Over a century of sinking in Mexico City: No hope for significant elevation and storage capacity recovery. *Journal of Geophysical Research: Solid Earth*, *126*(4), e2020JB020648. <https://doi.org/10.1029/2020jb020648>
- Chaussard, E., Milillo, P., Bürgmann, R., Perissin, D., Fielding, E. J., & Baker, B. (2017). Remote sensing of ground deformation for monitoring groundwater management practices: Application to the Santa Clara Valley during the 2012–2015 California drought. *Journal of Geophysical Research: Solid Earth*, *122*(10), 8566–8582. <https://doi.org/10.1002/2017jb014676>
- Chen, C., & Zebker, A. (2003). SNAPHU: Statistical cost, network-flow algorithm for phase unwrapping.
- Chen, J., Knight, R., & Zebker, H. A. (2017). The temporal and spatial variability of the confined aquifer head and storage properties in the San Luis Valley, Colorado inferred from multiple InSAR missions. *Water Resources Research*, *53*(11), 9708–9720. <https://doi.org/10.1002/2017wr020881>
- Chen, J., Knight, R., Zebker, H. A., & Schreüder, W. A. (2016). Confined aquifer head measurements and storage properties in the San Luis Valley, Colorado, from spaceborne InSAR observations. *Water Resources Research*, *52*(5), 3623–3636. <https://doi.org/10.1002/2015wr018466>
- Chen, Y., Liao, M., Wu, J., Li, X., Xiong, F., Liu, S., et al. (2022). Elastic and inelastic ground deformation in Shanghai Lingang area revealed by Sentinel-1, leveling, and groundwater level data. *Remote Sensing*, *14*(11), 2693. <https://doi.org/10.3390/rs14112693>

- Djamour, Y., Vernant, P., Nankali, H. R., & Tavakoli, F. (2011). NW Iran-eastern Turkey present-day kinematics: Results from the Iranian permanent GPS network. *Earth and Planetary Science Letters*, 307(1–2), 27–34. <https://doi.org/10.1016/j.epsl.2011.04.029>
- Ezquerro, P., Herrera, G., Marchamalo, M., Tomás, R., Béjar-Pizarro, M., & Martínez, R. (2014). A quasi-elastic aquifer deformational behavior: Madrid aquifer case study. *Journal of Hydrology*, 519, 1192–1204. <https://doi.org/10.1016/j.jhydrol.2014.08.040>
- Geological Survey of Iran. (1997). Retrieved from <https://gsi.ir/en>
- Goudarzi, M. A., Cocard, M., & Santerre, R. (2015). Noise behavior in CGPS position time series: The eastern North America case study. *Journal of Geodetic Science*, 5(1). <https://doi.org/10.1515/jogs-2015-0013>
- Gualandi, A., & Liu, Z. (2021). Variational Bayesian independent component analysis for InSAR displacement time-series with application to Central California, USA. *Journal of Geophysical Research: Solid Earth*, 126(4), e2020JB020845. <https://doi.org/10.1029/2020jb020845>
- Guzy, A., & Malinowska, A. A. (2020). State of the art and recent advancements in the modelling of land subsidence induced by groundwater withdrawal. *Water*, 12(7), 2051. <https://doi.org/10.3390/w12072051>
- Haghighi, M. H., & Motagh, M. (2019). Ground surface response to continuous compaction of aquifer system in Tehran, Iran: Results from a long-term multi-sensor InSAR analysis. *Remote Sensing of Environment*, 221, 534–550. <https://doi.org/10.1016/j.rse.2018.11.003>
- Herring, T., King, R., Floyd, M., & McClusky, S. (2015). *Introduction to GAMIT/GLOBK, release 10.6*. Department of Earth, Atmospheric and Planetary Science at MIT.
- Hersbach, H., Bell, B., Berrisford, P., Hirahara, S., Horányi, A., Muñoz-Sabater, J., et al. (2020). The ERA5 global reanalysis. *Quarterly Journal of the Royal Meteorological Society*, 146(730), 1999–2049. <https://doi.org/10.1002/qj.3803>
- Hoffmann, J., Galloway, D. L., & Zebker, H. A. (2003). Inverse modeling of interbed storage parameters using land subsidence observations, Antelope Valley, California. *Water Resources Research*, 39(2). <https://doi.org/10.1029/2001wr001252>
- Hoffmann, J., Zebker, H. A., Galloway, D. L., & Amelung, F. (2001). Seasonal subsidence and rebound in Las Vegas Valley, Nevada, observed by synthetic aperture radar interferometry. *Water Resources Research*, 37(6), 1551–1566. <https://doi.org/10.1029/2000wr900404>
- Hu, X., Lu, Z., & Wang, T. (2018). Characterization of hydrogeological properties in salt lake valley, Utah, using InSAR. *Journal of Geophysical Research: Earth Surface*, 123(6), 1257–1271. <https://doi.org/10.1029/2017jfo04497>
- Hyvärinen, A., & Oja, E. (1997). A fast fixed-point algorithm for independent component analysis. *Neural Computation*, 9(7), 1483–1492. <https://doi.org/10.1162/neco.1997.9.7.1483>
- Iran's WRM Co. (2014). Retrieved from <http://wrbs.wrm.ir/>
- Ireland, R. L., Poland, J. F., & Riley, F. S. (1984). *Land subsidence in the San Joaquin Valley, California, as of 1980*. US Government Printing Office.
- Jackson, D. A. (1993). Stopping rules in principal components analysis: A comparison of heuristical and statistical approaches. *Ecology*, 74(8), 2204–2214. <https://doi.org/10.2307/1939574>
- Jarvis, A., Reuter, H., Nelson, A., & Guevara, E. (2008). Hole-filled seamless SRTM data V4: International Centre for Tropical Agriculture (CIAT). Retrieved from <http://srtm.csi.cgiar.org>
- Jiang, L., Bai, L., Zhao, Y., Cao, G., Wang, H., & Sun, Q. (2018). Combining InSAR and hydraulic head measurements to estimate aquifer parameters and storage variations of confined aquifer system in Cangzhou, North China Plain. *Water Resources Research*, 54(10), 8234–8252. <https://doi.org/10.1029/2017wr022126>
- Jin, S., Wang, Q., & Dardanelli, G. (2022). A review on multi-GNSS for Earth observation and emerging applications. *Remote Sensing*, 14(16), 3930. <https://doi.org/10.3390/rs14163930>
- Jin, S., & Zhang, T. (2016). Terrestrial water storage anomalies associated with drought in southwestern USA from GPS observations. *Surveys in Geophysics*, 37(6), 1139–1156. <https://doi.org/10.1007/s10712-016-9385-z>
- Jolivet, R., Agram, P. S., Lin, N. Y., Simons, M., Doin, M. P., Peltzer, G., & Li, Z. (2014). Improving InSAR geodesy using global atmospheric models. *Journal of Geophysical Research: Solid Earth*, 119(3), 2324–2341. <https://doi.org/10.1002/2013jb010588>
- Jolivet, R., Grandin, R., Lasserre, C., Doin, M. P., & Peltzer, G. (2011). Systematic InSAR tropospheric phase delay corrections from global meteorological reanalysis data. *Geophysical Research Letters*, 38(17). <https://doi.org/10.1029/2011gl048757>
- Khorrani, M., Hatami, M., Alizadeh, B., Khorrani, H., Rahgozar, P., & Flood, I. (2019). Impact of ground subsidence on groundwater quality: A case study in Los Angeles, California. In *Computing in civil engineering 2019: Smart cities, sustainability, and resilience*. American Society of Civil Engineers Reston.
- Kumar, H., Syed, T. H., Amelung, F., Agrawal, R., & Venkatesh, A. (2022). Space-time evolution of land subsidence in the National Capital Region of India using ALOS-1 and Sentinel-1 SAR data: Evidence for groundwater overexploitation. *Journal of Hydrology*, 605, 127329. <https://doi.org/10.1016/j.jhydrol.2021.127329>
- Lees, M., Knight, R., & Smith, R. (2022). Development and application of a 1D compaction model to understand 65 years of subsidence in the San Joaquin Valley. *Water Resources Research*, 58(6), e2021WR031390. <https://doi.org/10.1029/2021wr031390>
- Li, G., Zhao, C., Wang, B., Peng, M., & Bai, L. (2023). Evolution of spatiotemporal ground deformation over 30 years in Xi'an, China, with multi-sensor SAR interferometry. *Journal of Hydrology*, 616, 128764. <https://doi.org/10.1016/j.jhydrol.2022.128764>
- Lu, Z., & Danskin, W. R. (2001). InSAR analysis of natural recharge to define structure of a ground-water basin, San Bernardino, California. *Geophysical Research Letters*, 28(13), 2661–2664. <https://doi.org/10.1029/2000gl012753>
- Marinkovic, P., & Larsen, Y. (2013). Consequences of long-term ASAR local oscillator frequency decay—An empirical study of 10 years of data.
- Meade, R. H. (1964). *Removal of water and rearrangement of particles during the compaction of clayey sediments*. US Government Printing Office.
- Miller, M. M., & Shirzaei, M. (2015). Spatiotemporal characterization of land subsidence and uplift in Phoenix using InSAR time series and wavelet transforms. *Journal of Geophysical Research: Solid Earth*, 120(8), 5822–5842. <https://doi.org/10.1002/2015jb012017>
- Miller, M. M., Shirzaei, M., & Argus, D. (2017). Aquifer mechanical properties and decelerated compaction in Tucson, Arizona. *Journal of Geophysical Research: Solid Earth*, 122(10), 8402–8416. <https://doi.org/10.1002/2017jb014531>
- Mirzadeh, S. M. J., Jin, S., Parizi, E., Chaussard, E., Bürgmann, R., Delgado Blasco, J. M., et al. (2021). Characterization of irreversible land subsidence in the Yazd-Ardakan Plain, Iran from 2003 to 2020 InSAR time series. *Journal of Geophysical Research: Solid Earth*, 126(11), e2021JB022258. <https://doi.org/10.1029/2021jb022258>
- Motagh, M., Shamsiri, R., Haghighi, M. H., Wetzel, H.-U., Akbari, B., Nahavandchi, H., et al. (2017). Quantifying groundwater exploitation induced subsidence in the Rafsanjan plain, southeastern Iran, using InSAR time-series and in situ measurements. *Engineering Geology*, 218, 134–151. <https://doi.org/10.1016/j.enggeo.2017.01.011>
- Najibi, N., & Jin, S. G. (2013). Physical reflectivity and polarization characteristics for snow and ice-covered surfaces interacting with GPS signals. *Remote Sensing*, 5(8), 4006–4030. <https://doi.org/10.3390/rs5084006>
- Ojha, C., Werth, S., & Shirzaei, M. (2019). Groundwater loss and aquifer system compaction in San Joaquin Valley during 2012–2015 drought. *Journal of Geophysical Research: Solid Earth*, 124(3), 3127–3143. <https://doi.org/10.1029/2018jb016083>

- Peng, M., Lu, Z., Zhao, C., Motagh, M., Bai, L., Conway, B. D., & Chen, H. (2022). Mapping land subsidence and aquifer system properties of the Willcox Basin, Arizona, from InSAR observations and independent component analysis. *Remote Sensing of Environment*, 271, 112894. <https://doi.org/10.1016/j.rse.2022.112894>
- Pepe, A., & Calò, F. (2017). A review of interferometric synthetic aperture RADAR (InSAR) multi-track approaches for the retrieval of Earth's surface displacements. *Applied Sciences*, 7(12), 1264. <https://doi.org/10.3390/app7121264>
- Pepe, A., & Lanari, R. (2006). On the extension of the minimum cost flow algorithm for phase unwrapping of multitemporal differential SAR interferograms. *IEEE Transactions on Geoscience and Remote Sensing*, 44(9), 2374–2383. <https://doi.org/10.1109/tgrs.2006.873207>
- Poland, J. F., & Ireland, R. (1988). *Land subsidence in the Santa Clara Valley, California, as of 1982*. Department of the Interior, US Geological Survey.
- Rezaei, A. (2018). Comments on “Quantifying groundwater exploitation induced subsidence in the Rafsanjan plain, southeastern Iran, using InSAR time-series and in situ measurements” by Motagh, M., Shamshiri, R., Haghighi, M.H., Wetzel, H.U., Akbari, B., Nahavandchi, H.,... & Arabi, S. [Engineering Geology, 218 (2017), 134–151]. *Engineering Geology*, 246, 417–419. <https://doi.org/10.1016/j.enggeo.2018.01.014>
- Rezaei, A., & Mousavi, Z. (2019). Characterization of land deformation, hydraulic head, and aquifer properties of the Gorgan confined aquifer, Iran, from InSAR observations. *Journal of Hydrology*, 579, 124196. <https://doi.org/10.1016/j.jhydrol.2019.124196>
- Rezaei, A., Mousavi, Z., Khorrami, F., & Nankali, H. (2020). Inelastic and elastic storage properties and daily hydraulic head estimates from continuous global positioning system (GPS) measurements in northern Iran. *Hydrogeology Journal*, 28(2), 657–672. <https://doi.org/10.1007/s10040-019-02092-y>
- Rigo, A., Béjar-Pizarro, M., & Martínez-Díaz, J. (2013). Monitoring of Guadalentín valley (southern Spain) through a fast SAR Interferometry method. *Journal of Applied Geophysics*, 91, 39–48. <https://doi.org/10.1016/j.jappgeo.2013.02.001>
- Riley, F. S. (1969). Analysis of borehole extensometer data from central California. *Land Subsidence*, 2, 423–431.
- Shahbazi, S., Mousavi, Z., & Rezaei, A. (2022). Constraints on the hydrogeological properties and land subsidence through GNSS and InSAR measurements and well data in Salmas plain, northwest of Urmia Lake, Iran. *Hydrogeology Journal*, 30(2), 533–555. <https://doi.org/10.1007/s10040-021-02416-x>
- Shepard, D. (1968). A two-dimensional interpolation function for irregularly-spaced data (pp. 517–524).
- Shi, X., Fang, R., Wu, J., Xu, H., Sun, Y., & Yu, J. (2012). Sustainable development and utilization of groundwater resources considering land subsidence in Suzhou, China. *Engineering Geology*, 124, 77–89. <https://doi.org/10.1016/j.enggeo.2011.10.005>
- Shi, X., Zhu, T., Tang, W., Jiang, M., Jiang, H., Yang, C., et al. (2022). Inferring decelerated land subsidence and groundwater storage dynamics in Tianjin–Langfang using Sentinel-1 InSAR. *International Journal of Digital Earth*, 15(1), 1526–1546. <https://doi.org/10.1080/17538947.2022.2122610>
- Smith, R., & Knight, R. (2019). Modeling land subsidence using InSAR and airborne electromagnetic data. *Water Resources Research*, 55(4), 2801–2819. <https://doi.org/10.1029/2018wr024185>
- Smith, R., & Li, J. (2021). Modeling elastic and inelastic pumping-induced deformation with incomplete water level records in Parowan Valley, Utah. *Journal of Hydrology*, 601, 126654. <https://doi.org/10.1016/j.jhydrol.2021.126654>
- Smith, R. G., Knight, R., Chen, J., Reeves, J. A., Zebker, H. A., Farr, T., & Liu, Z. (2017). Estimating the permanent loss of groundwater storage in the southern San Joaquin Valley, California. *Water Resources Research*, 53(3), 2133–2148. <https://doi.org/10.1002/2016wr019861>
- Sneed, M. (2001). *Hydraulic and mechanical properties affecting ground-water flow and aquifer-system compaction*. US Department of the Interior, US Geological Survey.
- Song, S., Bai, L., & Yang, C. (2022). Characterization of the land deformation induced by groundwater withdrawal and aquifer parameters using InSAR observations in the Xingtai Plain, China. *Remote Sensing*, 14(18), 4488. <https://doi.org/10.3390/rs14184488>
- TAMAB. (2004). *National groundwater resources status*. Basic Studies Office, Iran Water Resources Management Company.
- Tizzani, P., Bernardino, P., Casu, F., Euillades, P., Manzo, M., Ricciardi, G., et al. (2007). Surface deformation of Long Valley caldera and Mono Basin, California, investigated with the SBAS-InSAR approach. *Remote Sensing of Environment*, 108(3), 277–289. <https://doi.org/10.1016/j.rse.2006.11.015>
- Wang, B., Zhao, C., Zhang, Q., Lu, Z., & Pepe, A. (2021). Long-term continuously updated deformation time series from multisensor InSAR in Xi'an, China from 2007 to 2021. *IEEE Journal of Selected Topics in Applied Earth Observations and Remote Sensing*, 14, 7297–7309. <https://doi.org/10.1109/jstars.2021.3096996>
- Wilson, A. M., & Gorelick, S. (1996). The effects of pulsed pumping on land subsidence in the Santa Clara Valley, California. *Journal of Hydrology*, 174(3–4), 375–396. [https://doi.org/10.1016/0022-1694\(95\)02722-x](https://doi.org/10.1016/0022-1694(95)02722-x)
- Wright, T. J., Parsons, B. E., & Lu, Z. (2004). Toward mapping surface deformation in three dimensions using InSAR. *Geophysical Research Letters*, 31(1), L01607. <https://doi.org/10.1029/2003gl018827>
- Yunjun, Z., Fattahi, H., & Amelung, F. (2019). Small baseline InSAR time series analysis: Unwrapping error correction and noise reduction. *Computers & Geosciences*, 133, 104331. <https://doi.org/10.1016/j.cageo.2019.104331>
- Zhu, K., Zhang, X., Sun, Q., Wang, H., & Hu, J. (2022). Characterizing Spatiotemporal Patterns of Land Deformation in the Santa Ana Basin, Los Angeles, from InSAR Time Series and Independent Component Analysis. *Remote Sensing*, 14(11), 2624. <https://doi.org/10.3390/rs14112624>